Quantification of structural and microvascular changes for diagnosing early-stage oral cancer

PING-HSIEN CHEN,[1,2,3,9] YU-JU CHEN,[3,9] YI-FEN CHEN,[4] YI-CHEN YEH,[2,5] KUO-WEI CHANG,[4,6,7] MING-CHIH HOU,[2,8] AND WEN-CHUAN KUO[3,*]

[1]*Endoscopy Center for Diagnosis and Treatment, Taipei Veterans General Hospital, Taipei 112, Taiwan*
[2]*Department of Medicine, National Yang-Ming University, Taipei 112, Taiwan*
[3]*Institute of Biophotonics, National Yang-Ming University, Taipei 112, Taiwan*
[4]*Institute of Oral Biology, National Yang-Ming University, Taipei 112, Taiwan*
[5]*Department of Pathology and Laboratory Medicine, Taipei Veterans General Hospital, Taipei 112, Taiwan*
[6]*Department of Dentistry, National Yang-Ming University, Taipei 112, Taiwan*
[7]*Department of Stomatology, Taipei Veterans General Hospital, Taipei 112, Taiwan*
[8]*Department of Medicine, Taipei Veterans General Hospital, Taipei 112, Taiwan*
[9]*These authors contributed equally to this work*
[*]*wckuo@ym.edu.tw*

Abstract: Changes in mucosal microvascular networks, called intraepithelial papillary capillary loops (IPCL), are an important key factor for diagnosing early-stage oral cancer *in vivo*. Nevertheless, there are a lack of tools to quantify these changes objectively. This is the first study to quantify the IPCL changes *in vivo* to differentiate benign or malignant oral lesions by the optical coherence tomography (OCT) technique. K14-EGFP-miR-211-GFP transgenic mice were inducted by 4-Nitroquinoline-1-oxide to produce oral carcinogenesis in different stages, including normal, premalignancy and cancer. The results showed significant differentiation between benign or malignant lesions by OCT quantitative parameters, including epithelial thickness, IPCL density, radius and tortuosity.

1. Introduction

Change in the mucosal microvascular networks, called intraepithelial papillary capillary loops (IPCLs), is a key factor for diagnosing oral and esophageal squamous cell carcinoma (SCC) in the early stage. Magnifying endoscopy with narrow-band imaging (ME-NBI) is the most popular technique to observe the change in the IPCL *in vivo* and has been broadly used in the diagnosis of esophageal SCC [1]. Its use in oral SCC has also been studied in a small series with sensitivity of 75.7% and specificity of 91.5% [2,3]. However, this method has some limitations and restricted clinical use, especially in the oral cavity. First, characterizing IPCL under ME-NBI is subjective; the accuracy relies on the operator's experience and is prone to significant variation [4]. Thus, the requirement for computer-assisted diagnosis (CAD) to overcome this subjectivity had increased in recent years [5]. Second, the penetration of NBI is influenced by hyperkeratinization, increased epithelium thickness/stratification, and the presence of lymphoid tissue, which are common in the oral cavity [6]. Third, the operation of the magnifying endoscope requires skill. Imprecise operation can cause mucosal bleeding and reduce the image quality.

Optical coherence tomography (OCT) is an evolving imaging technology for label-free and radiation-free imaging [7]. It can provide real-time cross-sectional tomography images and three-dimensional (3D) reconstruction images with high-resolution (10–20 μm) and adequate tissue penetration depth (1.5–2 mm). Its application in oncology has expanded in recent years [8]. In addition to conventional structural images, OCT angiography (OCTA) further generates 3D depth-resolved vascular images *in vivo* by using endogenous motion contrast [9]. It has

successfully imaged oral IPCL in normal and benign ulcerative oral mucosa [10,11]. In our previous performed pilot study, we advanced this technique to image oral cancerous IPCL in mice model, and the result was identical to that of ME-NBI [12]. In comparison with ME-NBI, OCTA has the advantages of deeper penetration, easier non-contact operation, rapid and continuous scanning over a large field of view, 3D nature, and most importantly, the ability of quantification, which can lead to objective diagnostic parameters in the future.

The search for quantitative parameters for disease diagnosis is an important issue for the recent development of automated CAD. Several quantitative OCT parameters have been proposed in oral oncology research, such as change in the epithelial thickness, standard deviation of the intensity, and other optical scattering properties [13,14]. The advantage of quantitative parameters is the ability to identify subtle variations, which are difficult to detect by unaided eyes. This is especially important in the detection of early cancerous change. Different parameters can be further combined to increase the diagnostic accuracy. However, current quantitative parameters are based on backscattered intensity properties obtained from few selected A-line or B-scan images. A tumor is heterogeneous in nature, resulting in bias in such selective analysis. In addition, the accuracy of backscattered intensity properties, such as epithelial thickness, decay constant, or standard deviation evaluation, are easily influenced by structural variation of the oral cavity, strong backscattered signal from the tissue interfaces, and the selected depth range of the analysis [15–17]. There continues to be a lack of quantitative parameters based on the IPCL change, which is considered the most potentially powerful indicator for diagnosing early-stage oral cancer and avoiding structural variation. Therefore, the first aim of this study is to quantify the IPCL changes in different stages of carcinogenesis by the OCTA technique. The second aim is to statistically compare different quantitative parameters, including epithelial thickness, standard deviation of intensity, and IPCL change, in different stages of carcinogenesis. Finally, we aim to propose a new OCT diagnostic process to help physicians diagnose early-stage oral SCC quickly and intuitively.

2. Materials and methods

2.1. Animal and experimental protocol

The K14-EGFP-miR-211-GFP transgenic mice, generated by Chang et al., were used in this study. These mice have the advantage of high potential for oral cancer induction, and early-stage cancer on the tongue surface can be intensified by the expression of K14-EGFP-miR-211-GFP [18].

4-Nitroquinoline-1-oxide (4NQO), a water-soluble quinoline derivative, which forms DNA adducts and induces intracellular oxidative stress, can result in mutations and breakage of the DNA strand. It can be a carcinogen to induce oral SCC similar to the carcinogenesis provoked by tobacco exposure. The pathological pathway also resembles human oral SCC, including the progression from hyperplasia, dysplasia, and carcinoma in situ (CIS) to SCC [19].

In this study, 100 µg/mL of water-soluble 4NQO (Sigma-Aldrich, St. Louis, MO, USA) was added to the drinking water of 6-weeks-old K14-EGFP-miR-211-GFP transgenic mice for 12 weeks. The experiments were performed on weeks 20, 24, and 28 after the commencement of cancer induction (Fig. 1(A)). The steps of the experiment were as follows: 1. the mouse was anesthetized by intraperitoneal injection of 2,2,2 tribromoethanol (200 mg/kg). 2. The tip of the tongue was gently extended, fixed, and scanned by OCT *in-vivo* (Fig. 1(B), top picture). 3. After image acquisition, the mouse was sacrificed, and the tongue was severed. The severed tongue was scanned by a fluorescent system (LT-9900 Illumatool bright light) to identify the green area, which indicated a potential tumor (the expression of K14-EGFP-miR-211-GFP) (Fig. 1(B), lower left picture). The green area was then inked (Fig. 1(B), lower right picture). 4. Histological sections were made at the inked area (black dotted line on Fig. 1(B), lower right picture) and stained with H&E. The slides were assessed by experienced pathologists (Dr. Yi-Chen Yeh and Professor Kuo-Wei Chang), and the results were classified as normal,

premalignant change (hyperplasia to low-grade dysplasia), and cancerous change (high-grade dysplasia to SCC) (Fig. 1(C)). 5. Finally, the corresponding OCT imaging and histological results were compared. All experiments were approved by the Institution for Animal Care and Use Committee at National Yang-Ming University.
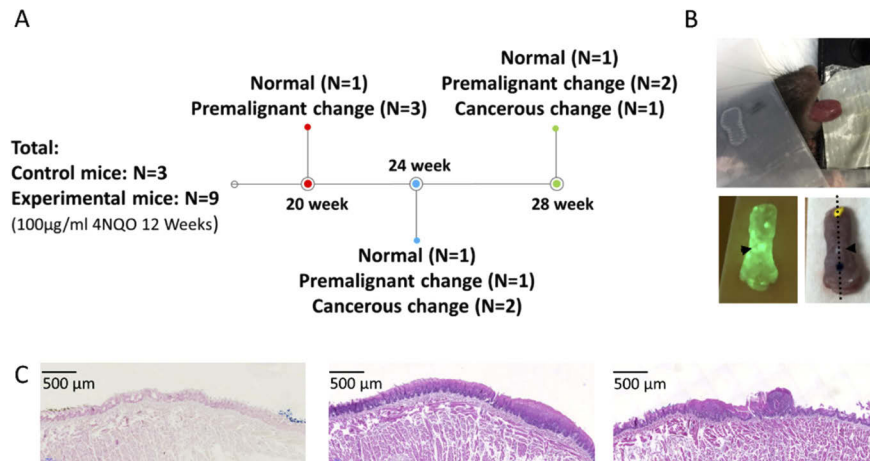

Fig. 1. Experimental protocol. (A) Experimental schedule, number of mice (N), and histology results. (B) Upper picture: OCT scanning of tip of tongue *in vivo* (X-Y: 4×4 mm); lower left picture: fluorescence imaging to identify the green area, which indicates a potential tumor (black arrowhead); lower right picture: inking of the potential tumor and histological sectioning on black dotted line. (C) Histology definition: normal (left), premalignant change, including hyperplasia to low-grade dysplasia (middle), and cancerous change, including high-grade dysplasia to SCC (right).

2.2. Setup of the OCT system

The spectral-domain OCT system was used in this study. The light source was a supercontinuum laser with a central wavelength of 1275 nm and spectral bandwidth of 200 nm. A 50/50 coupler was arranged to split the light power into 50% incident power for the reference mirror (with an attenuator) and the remaining 50% incident power (i.e., ∼6 mW) focused on a scanning spot. After the recombination of the sample and reference beams, the light was focused on a line-scan spectrometer (2048 pixels, Wasatch Photonics) for detection, and the data were transferred to a computer. After the data acquisition, resampling from λ to a specified k space was performed on each spectrum to ensure that the spectrum was linearly interpolated in k-space [20]. Then, dispersion compensation was used to ensure the signal could be accurately recovered to the depth profile after fast Fourier transform (FFT) of the spectral interferogram [21]. The maximum image acquisition rate, 76 frames per second (900×1024 pixels in the X-Z plane), was based on the integration time setting in a line-scan spectrometer and the scanning speed of the X-Y galvanometer scanner. The axial system resolution in air was measured as ∼5 μm by using a mirror with an attenuator as a sample. A 1951 USAF resolution test target (Edmund Optics) was used as the standard resolution test sample for measurement of the lateral resolution, confirming that the lateral resolution of the OCT setup was approximately 7 μm.

2.3. Process of structural and OCTA imaging

After the acquisition of the spectral interferograms, the structural images and OCTA images were numerically analyzed. The structural images were displayed on a logarithmic grayscale in a two-dimensional (2D) format, and a 3D image was a volume of $4\,mm \times 4\,mm \times 3\,mm$

corresponding to $900 \times 400 \times 1024$ pixels in the X, Y, and Z directions. Different viewing angles can be reconstructed by the 3D visualization framework software (Avizo 6.1). The OCTA images were analyzed based on the amplitude variance. By calculating the amplitude term in the autocorrelation algorithm between B-scans (i.e., inter-frame calculation), the coefficient can be expressed as

$$\sigma^2 = 1 - \sum_{y_j=1}^{J} \sum_{z=1}^{I} \left| A_{x,y_j,z} \right| \left| A_{x,y_{j+1},z} \right| / \sum_{y_j=1}^{J} \sum_{z=1}^{I} \left(\frac{|A_{x,y_j,z}|^2 + |A_{x,y_{j+1},z}|^2}{2} \right). \tag{1}$$

Here, x, y, and z are the spatial pixel coordinates corresponding to the fast and slow scanning axes and the depth coordinate, respectively. $|A_{x,y_j,z}|$ is the amplitude of the complex-valued OCT data of the jth B-scan. $J = 4$ is the number of averaged B-scans, and $I = 4$ is the number of averaged depth pixels. Vascular contrast was achieved because the flow regions and bulk tissue had very different correlation values. Detailed mathematical descriptions are provided in [22].

2.4. Quantitative analysis of OCT images

Because the dysplastic cells are present only in the epithelium (EP) in the early stage of oral carcinogenesis, the analysis of change in the EP is reasonable for detecting dysplasia or early
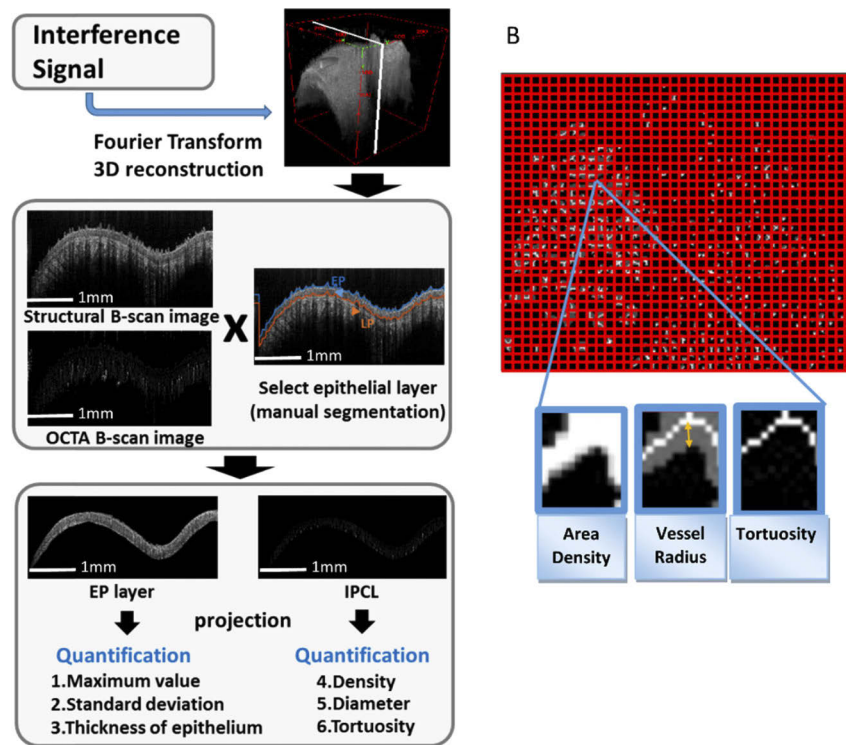

Fig. 2. Analysis of OCT image. (A) Flow chart of image processing and quantitative analysis: manual segmentation was performed to select the epithelium layer; then, three quantitative parameters from the structural image and three parameters from the OCTA image (IPCL) were analyzed. (B) Definition of IPCL parameters: vessel area density (ratio): area of vessels (white area) / entire area (window size 30×30 pixels); average vessel radius (number of pixels): distance from vessel margin to central skeleton (orange double arrow) (window size 30×30 pixels); tortuosity: entropy calculated from the skeletonized vessel map (window size 10×10 pixels).

cancer. Thus, after the imaging process, we manually separated the EP from the boundary between EP and lamina propria (LP) in the intensity B-scan image. In the case of the structural image, three known parameters, namely, maximum value projection, standard deviation of intensity [23], and epithelial thickness [15], were calculated from the A-lines. In the case of the OCTA image, the *en-face* maximum intensity projection image of the EP layer was used to present an IPCL image as that obtained in ME-NBI. Then, three parameters of the IPCLs, namely, vessel area density, average vessel radius, and tortuosity were calculated from the individualized window size. Finally, the values of the quantitative parameters were presented in *en-face* maps for easy interpretation (Fig. 2(A)).

Vessel area density is defined as the ratio of the area of the vessels in the projection view to the area of the imaging region. By using the Euclidean distance transform [24] of the binarized vessel *en-face* projection map, the distance from each pixel in a binarized map to the pixel locations that approximate the centerline of the blood vessels (i.e., vessel skeleton) was counted in number of pixels and then averaged within each window as the average vessel radius (unit: number of pixels). Here, the threshold of the binarized vessel map was determined by using Otsu algorithm. Otsu is an automatic threshold selection based segmentation method, which chooses a threshold that minimizes the intraclass variance of the thresholded black and white pixels [25]. Furthermore, the same window size (30×30 pixels) was used throughout the study. Finally, the results were shown in color scale to highlight the regions with greater radius. Bendiness was determined by calculating the vessel tortuosity [26] of the skeletonized vessel *en-face* projection map (no unit). Larger tortuosity entropy corresponds to a more tortuous and "wiggly" vessel trajectory [27] (Fig. 2(B)). All parameters were automatically calculated using a program written in MATLAB (MathWorks) and were compared statistically for different carcinogenesis stages by Mann–Whitney U test (SPSS Version 22).

3. Results

3.1. Animal (N) and histology results

Three control mice and nine 4NQO-induced mice were studied. The progression of carcinogenesis in different weeks is shown in Fig. 1(A). Overall, three control mice showed normal histology, six experimental mice presented premalignant change, and three experimental mice developed cancerous change.

3.2. En-face IPCL images and quantitative maps of different carcinogenesis stages

One control mouse, three premalignant mice, and three cancerous mice are presented in Fig. 3. The original *en-face* IPCL images (scanning area: 4×4 mm) and magnified IPCL images are presented in Fig. 3(A), (B). From normal to premalignant to cancerous change, the morphology of the IPCL progressed from small and closed loops with a regular shape to large and open loops with an irregular shape (B), which is identical to the observation reported in our previous study [12]. The quantitative IPCL maps of vessel area density, radius and tortuosity in different carcinogenesis stages are shown in Fig. 3(C-E). By comparing the image of the premalignant change with that of the control, an increasing trend of the vessel density, radius, and tortuosity can be observed. The histology of premalignant mice showed increased thickness of the epithelial layer with basal cell hyperplasia (F). By comparing the cancerous change with the control and premalignant change, significant changes in the vessel density, radius, and tortuosity were noted along with prominent red areas, especially in the density and radius maps. The histology of the red area showed dysplastic changes in the full thickness of the epithelium lining, which indicated early malignancy (F). For further confirming the relationship between IPCL change and histology, we measured the tumor diameter on the IPCL image (A) and compared it with the tumor diameter

in the histology images (F). The results showed identical tumor diameters with disparity of less than 50 μm.

3.3. Statistical comparison of quantitative parameters in different carcinogenesis stages

In order to avoid selection bias originating from using only few A-lines or B-scan images, we included datasets from all scanning areas into the analysis. The first step was to define the pathogenesis of the scanning area. In control mice and mice with premalignant change, the entire scanning area and datasets were labeled as normal or premalignant change based on histology. In mice with cancerous change, the cancer area was circled based on the *en-face* IPCL image because of similar tumor diameters in the IPCL and histology images in Fig. 3(A) and 3(F). For example, Fig. 4(A) shows a tongue with cancerous lesions (the same case in Fig. 3: cancerous change-mouse 2). The cancerous area is circled by an orange line, and the diameter of the tumor is approximately 1.66 mm. The corresponding histology is squamous cell carcinoma with diameter of approximately 1.70 mm (Fig. 4(B), corresponding to orange dotted line in Fig. 4(A)). Therefore, this area was labeled as cancerous change in the dataset. The remnant scanning area is circled by a white line and the corresponding histology is hyperplasia (Fig. 4(C), corresponding to green dotted line in Fig. 4(A)). This dataset was labeled as premalignant change. Finally, 3 datasets (n) were labeled as normal, 9 datasets were labeled as premalignant change, and 3 datasets were labeled as cancerous change. The median value and interquartile range of the quantitative parameters, including the IPCL parameters (density, radius, tortuosity) and structural parameters (maximum projection (MP) of intensity, standard deviation (STD) of intensity, epithelial thickness), from each dataset were calculated and compared for different carcinogenesis stages.

The three IPCL parameters revealed a sequential increase in the IPCL density, radius, and tortuosity from normal to premalignant change to cancerous change ($p < 0.05$). However, the structural parameters showed only a significant increase in the epithelial thickness from normal to cancerous lesions (Fig. 4(D)).

3.4. New process for diagnosing and staging early oral cancer in vivo

The identification of the morphological change in IPCL using a magnified image is helpful in differentiating between benign and malignant oral lesions *in vivo*, but the field of view is small. Studying numerous magnified images with large screen area is labor-intensive. The quantification of the IPCL or structural change can help detect these changes with less effort and make the identification more objective. For example, Fig. 5 shows a new flow chart to diagnose and stage early oral SCC. In the first step, the quantitative parameters are calculated and presented in *en-face* quantitative maps, which can help the physician understand the quantitative change easily and identify the tumor area intuitively. As in Fig. 5(A), the red area indicating potential malignancy can be identified clearly in the IPCL density, radius, and tortuosity maps and in the epithelial thickness map. The second step is to obtain the magnified IPCL image and cross-sectional tomography image of this red area. We can confirm the malignancy diagnosis based on the IPCL morphology (large and open loops), as seen in the IPCL image in Fig. 5(B). The cross-sectional tomography image in Fig. 5(C) shows the diameter of the tumor as approximately 1.88 mm, and destruction of the basement membrane with a depth of invasion of approximately 0.25 mm was observed on the OCT image. The histological results, which showed the tumor diameter as approximately 1.7 mm and depth of invasion as approximately 0.2 mm (Fig. 5(D)), were compatible with the results of the OCT image. In this new pathway, the detection, diagnosis, and staging can be performed in one OCT scanning.
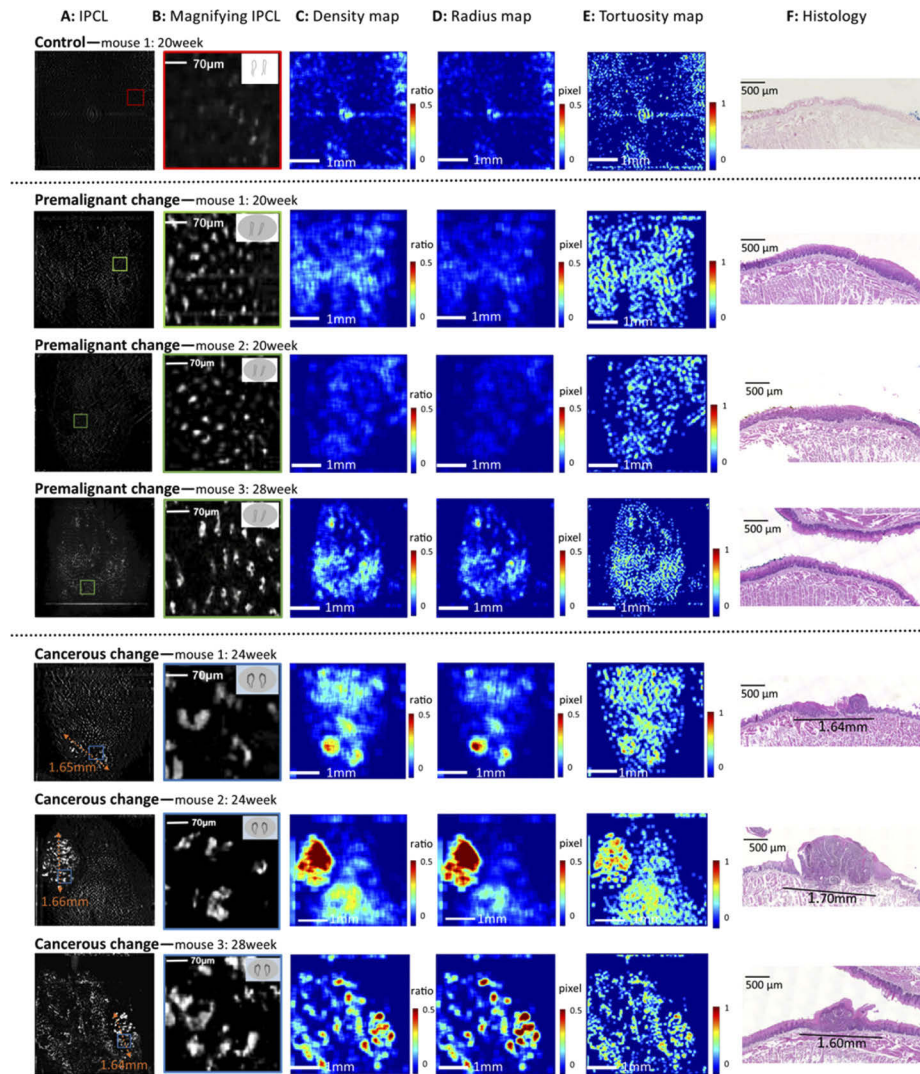
Fig. 3. *En-face* IPCL images, quantitative maps, and histology results. **Control:** (A) Few vessels in *en-face* IPCL image (A: 4×4 mm field of view). (B) Magnified image of the IPCLs (corresponding to the red square in A) showed small and closed loops with regular shapes. (C–E) Quantitative maps of density, radius, and tortuosity show blue backgrounds without red areas. (F) Histology is normal. **Premalignant change (three mice):** (A) Higher number of vessels than in the control. (B) Magnified image of the IPCLs (corresponding to green square in A) showed elongated and closed loops with regular shapes. (C–E) Quantitative maps showed increasing trends of density, radius, and tortuosity when compared with the control. (F) Histology showed increased thickness of the epithelial layer with basal cell hyperplasia. **Cancerous change (three mice):** (A) Significant increase in number and size of vessels. The orange double-arrow dotted line shows the measured tumor diameter on the IPCL image. (B) Magnified image of the IPCLs (corresponding to blue square in A) shows large open loops with irregular shapes. (C–E) Quantitative maps show significantly increased density, radius, and tortuosity with prominent red areas, especially in the density and radius maps. (F) Histology of the red area shows dysplastic changes in full thickness of the epithelium lining, which indicates early malignancy. The tumor diameter in the histology image is identical to that in the IPCL image (A). (The top right corners of the images in B show the Inoue classification of the IPCL for diagnosing SCC [1].)
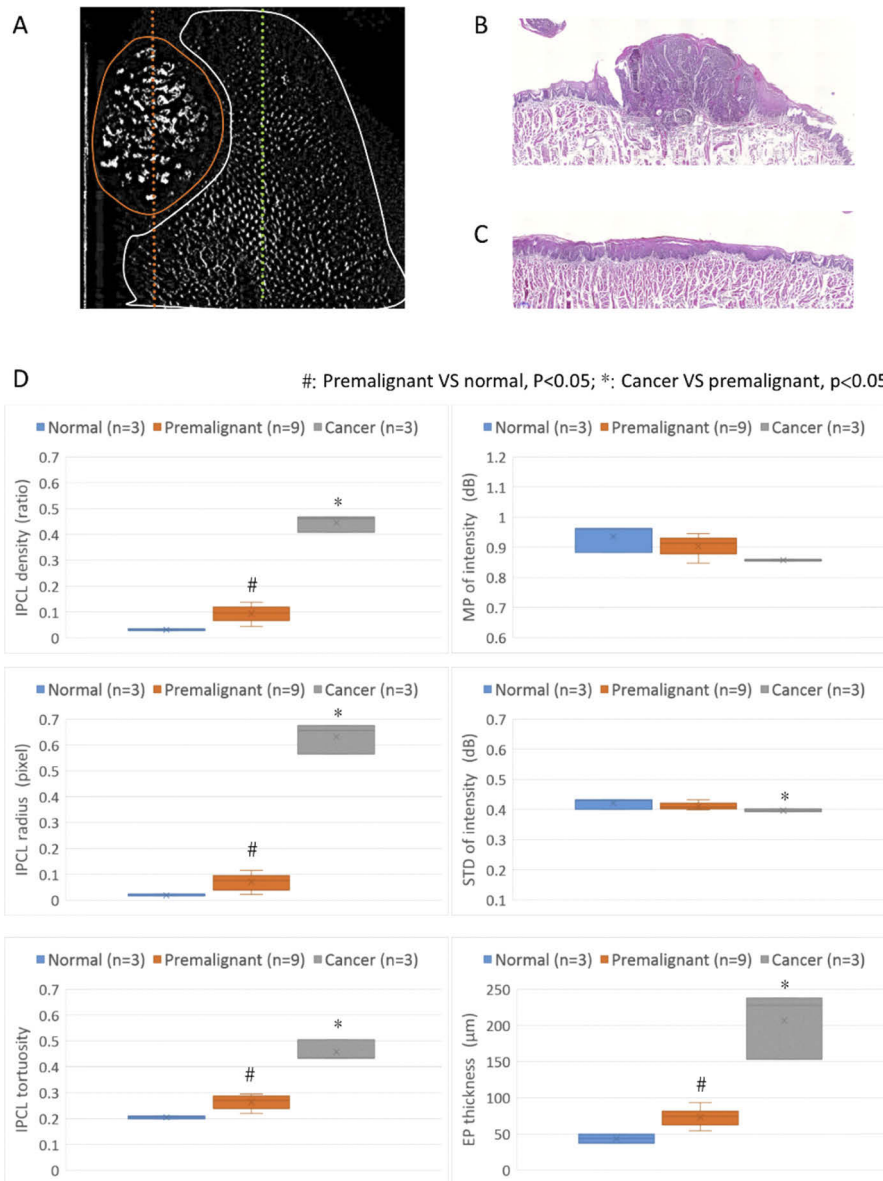
Fig. 4. Diagnostic ability of different quantitative parameters. (A) *En-face* IPCL image: the area circled by the orange line was labeled as cancerous area, and the histology corresponding to the orange dotted line showed SCC (B); The area circled by the white line was labeled as premalignant area, and the histology corresponding to the green dotted line showed hyperplasia (C). (D) Statistical comparison of quantitative parameters in different stages of carcinogenesis (center line of boxplot: median; x of boxplot: mean): sequential increase in IPCL density, radius, and tortuosity and increase in epithelial thickness from normal to premalignant change to cancerous change (p < 0.05) (MP: maximal projection; STD: standard deviation; EP: epithelial layer).
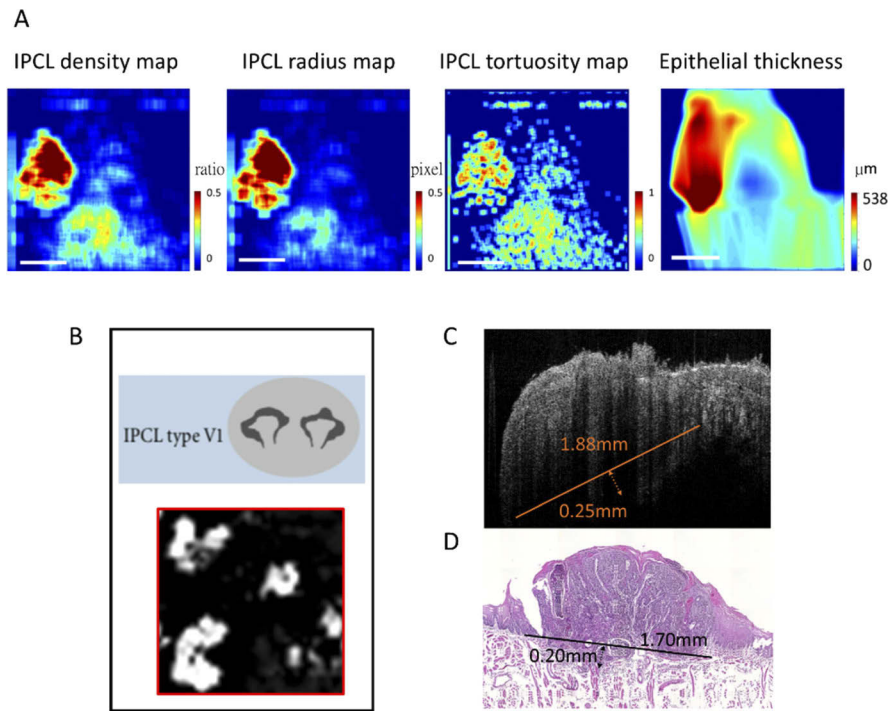
Fig. 5. New method for diagnosing and staging early oral cancer. (A) After OCT scanning, the quantitative parameters can be calculated and presented as *en-face* quantitative maps. Using the IPCL density, radius and tortuosity maps and the epithelial thickness map, we can intuitively locate the red area indicating potential malignancy. (B) The magnified IPCL image of the red area showed large open loops with irregular shapes, which indicated cancerous change. (C) A cross-sectional tomography image of the red area showed a tumor with destruction of the basement membrane and depth of invasion of approximately 0.25 mm. The diameter of the tumor was estimated at approximately 1.88 mm. (D) Corresponding histology of the red area was SCC with superficial stromal invasion up to approximately 0.20 mm. The diameter of the tumor was approximately 1.70 mm, which was compatible with the result of the OCT image.

4. Discussion

Early detection and diagnosis of oral SCC are difficult in the current screening program [28]. Up to 50% of oral cancers are not detected until the disease is well advanced [29]. The major challenge is "field cancerization" in the oral cavity, caused by exposure to carcinogens, such as cigarettes or alcohol, which can produce multiple potentially malignant disorders (PMDs), such as oral erythroplakias, leukoplakias, and lichenoid disorders. Most PMDs are benign, but the mean overall malignant transformation rate is approximately 12.1% if dysplasia appears [30]. To date, the identification of all PMDs and accurate prediction of the PMDs that would develop oral SCC remains a challenge. The use of adjunctive tools such as toluidine blue, chemiluminescence, or tissue fluorescence imaging in addition to visual examination can help identify PMDs, but cannot differentiate between benign tissue or malignancy accurately because of high false-positive rate [31]. Tissue biopsy remains the gold standard for diagnosing PMDs, but this procedure is invasive, uncomfortable, and expensive in the case of multiple PMDs. The reliability of the biopsy is also doubtful. According to current evidence, up to ~10% of oral lesions contained malignant or dysplastic changes although preoperative biopsy results were negative [32]. Recently, the use of

optical tools such as ME-NBI to differentiate between benign and early cancerous lesions *in vivo* and guide tissue biopsy in oral and esophageal diseases has grown rapidly [1–3,33]. However, the use of this method in oral cancer screening is limited because of the difficult operation and shallow penetration depth of ME-NBI. To obtain a magnified IPCL morphology for diagnosis, a special magnifying endoscope should be touched softly on the oral mucosa, which will cause discomfort and induce retching. If a large screening area is required, the operator should move the endoscope continuously and steadily while maintaining a close distance of approximately 2 mm between the oral mucosa and lens. This is a difficult and time consuming process. Moreover, the quality of the magnified image depends on the operator's skill, which influences the diagnosis.

In comparison with ME-NBI, OCT has deeper penetration depth and provides visualization of the full epithelial thickness and superficial connective tissue for diagnosis and staging of early cancerous lesion. Its non-contact and non-contrast properties also make OCT easy to operate and reproduce. However, the application of OCT in oral oncology has not been well established. Through our series studies, we propose a new OCT image analysis method and diagnostic process for early-stage oral SCC. The first step is to present the IPCL morphology clearly using the OCTA technique. Based on this (Fig. 3) and our previous study [12], the IPCL morphology was found to change sequentially from small closed loops with regular shapes to large open loops with irregular shapes for the progression from normal tissue to dysplasia to cancerous lesions. The result of these studies showed that the OCTA technique is reproducible, and the change of IPCL is identical to current opinion on ME-NBI [1–3,33], which can be directly applied in oral or esophageal cancer diagnosis. The second important step is to quantify the IPCL change *in vivo*, which cannot be achieved by other tools, including ME-NBI. Three parameters, namely, the IPCL density, radius, and tortuosity, showed significant increase in their values for normal to dysplasia to early cancerous lesions (Fig. 4). These results are compatible with the histological results [34]. The importance of quantification is that unlike subjective morphology, it provides objective parameters, which can avoid diagnostic variation arising from difference in the experience levels of the physicians [4] and provide the information to develop CAD in the future. In comparison with other quantitative parameters relating to backscattering intensity properties, the IPCL parameters showed better ability to differentiate between benign and malignant lesions. The results of the standard deviation of intensity in our study were different from those in other studies [23] owing to the following two reasons. First, we considered all A-lines of the tumor area in the analysis; this was different from the procedure followed in previous studies, which selected A-lines or B-scan images. We believe this new method is more effective in presenting the heterogeneity of the malignancy to avoid selection bias. Second, a strong backscattered signal from the papilla of the tongue surface was found in our study, which was regarded as significant interference while calculating the maximal projection or standard deviation of the intensity [17]. Although the epithelial thickness was a useful structural parameter for differentiating between benign or malignant lesions, its accuracy alone may be affected by anatomical variation of the oral cavity and occasionally by epithelial atrophy in pathogenesis of human oral SCC [16,35]. Nevertheless, we cannot determine the best diagnostic parameter in this study because of lack of direct comparison of these parameters in a validation group. In conclusion, quantitative analysis of the OCT image is useful in differentiating between benign and malignant oral lesions. The combination of different quantitative parameters, including IPCL or backscattered intensity parameters, may be a better way to improve diagnostic accuracy in the future.

The third significant step of our study is a new diagnostic pathway for oral cancer by the integration of the above two steps. The quantitative information is presented in *en-face* maps to enable the physician to understand the change easily and identify the potential tumor area intuitively, as shown in Fig. 5(A). Further, the diagnosis and staging can be performed simultaneously by magnified IPCL morphology and tomography images of the red area, as in Fig. 5(B) and 5(C). In this pathway, doctors are required to examine only the potential malignant

area marked by enhanced contrast, which saves time spent on the screening program. After the collection of an extensive human database in the future, the presentation of potential tumor areas can be further aided by computers based on this quantitative method. Another interesting outcome of this study is the ability to measure the depth of tumor invasion (DOI) by OCT. DOI is a new important prognostic factor for early-stage oral cancer, but a standard method to measure it in the pre-operation stage is lacking [36,37]. OCT has the advantage of better axial resolution than ultrasound, CT, and MRI, and it has shown better T-stage evaluation in early-stage esophageal cancer [38]. Several studies have already presented the ability of OCT to evaluate the intactness of basement membrane in oral cancer, but studies on evaluating the DOI are lacking. In our study, we demonstrated one case of evaluating the DOI by OCT, which was compatible with histology (Fig. 5(C) and 5(D)). It is too early to conclude that OCT is suitable for measuring the DOI because of the small sample size in this study. Nevertheless, it encourages the use of OCT technique for diagnosing and predicting the prognosis of early cancer *in vivo* in the future.

There are several limitations of this study. First, a small sample size and absence of a validation group prevents the comparison of different quantitative parameters and calculations of the diagnostic cut-off value, sensitivity, and specificity. The pathological nature of animals and humans is different. Therefore, large human based studies to validate these results are needed. Second, the tumor margin was defined based on the IPCL image, which is not evident well under current knowledge. However, in a clinical environment, the determination of the tumor margin by ME-NBI to observe the IPCL morphology *in-vivo* is a popular procedure during endoscopic resection. The tumor diameter measured on the IPCL image was similar to the histology of three cancerous mice in our study (Fig. 3). Therefore, we believe that our proposed method is an acceptable experimental method.

5. Conclusion

OCT is a non-invasive and reproducible technique to present oral IPCL *in vivo*. Quantitative analysis of the IPCL change, including density, radius, and tortuosity, can be objective indicators for diagnosing early-stage oral SCC. We believe that this method can be applied in human studies because the animal results currently obtained in this work are compatible with known histological changes in human oral SCC. Further studies to validate these results in human participants are needed to establish the accuracy or cut-off value of these new quantitative parameters for diagnosing early-stage oral SCC, which will enable this method to achieve clinical utility.

Disclosures

The authors declare no conflicts of interest.

References

1. H. Inoue, M. Kaga, H. Ikeda, C. Sato, H. Sato, H. Minami, E. G. Santi, B. Hayee, and N. Eleftheriadis, "Magnification endoscopy in esophageal squamous cell carcinoma: a review of the intrapapillary capillary loop classification," Ann Gastroenterol **28**(1), 41–48 (2015).
2. A. Vu and C. S. Farah, "Narrow band imaging: clinical applications in oral and oropharyngeal cancer," Oral Dis. **22**(5), 383–390 (2016).
3. U. H. Ansari, E. Wong, M. Smith, N. Singh, C. E. Palme, M. C. Smith, and F. Riffat, "Validity of narrow band imaging in the detection of oral and oropharyngeal malignant lesions: A systematic review and meta-analysis," Head Neck **41**(7), 2430–2440 (2019).

4. C. Piazza, D. Cocco, F. Del Bon, S. Mangili, P. Nicolai, and G. Peretti, "Narrow band imaging and high definition television in the endoscopic evaluation of upper aero-digestive tract cancer," Acta Otorhinolaryngol. Ital. **31**(2), 70–75 (2011).

5. Y. Y. Zhao, D. X. Xue, Y. L. Wang, R. Zhang, B. Sun, Y. P. Cai, H. Feng, Y. Cai, and J. M. Xu, "Computer-assisted diagnosis of early esophageal squamous cell carcinoma using narrow-band imaging magnifying endoscopy," Endoscopy **51**(04), 333–341 (2019).

6. Y. C. Lin, W. H. Wang, K. F. Lee, W. C. Tsai, and H. H. Weng, "Value of narrow band imaging endoscopy in early mucosal head and neck cancer," Head Neck **34**(11), 1574–1579 (2012).

7. D. Huang, E. A. Swanson, C. P. Lin, J. S. Schuman, W. G. Stinson, W. Chang, M. R. Hee, T. Flotte, K. Gregory, C. A. Puliafito, and J. G. Fujimoto, "Optical coherence tomography," Science **254**(5035), 1178–1181 (1991).

8. J. Wang, Y. Xu, and S. A. Boppart, "Review of optical coherence tomography in oncology," J. Biomed. Opt. **22**(12), 1–23 (2017).

9. A. Zhang, Q. Zhang, C. L. Chen, and R. K. Wang, "Methods and algorithms for optical coherence tomography-based angiography: a review and comparison," J. Biomed. Opt. **20**(10), 100901 (2015).

10. W. Wei, W. J. Choi, and R. K. Wang, "Microvascular imaging and monitoring of human oral cavity lesions in vivo by swept-source OCT-based angiography," Lasers Med. Sci. **33**(1), 123–134 (2018).

11. W. J. Choi and R. K. Wang, "In vivo imaging of functional microvasculature within tissue beds of oral and nasal cavities by swept-source optical coherence tomography with a forward/side-viewing probe," Biomed. Opt. Express **5**(8), 2620–2634 (2014).

12. P. H. Chen, C. H. Wu, Y. F. Chen, Y. C. Yeh, B. H. Lin, K. W. Chang, P. Y. Lai, M. C. Hou, C. L. Lu, and W. C. Kuo, "Combination of structural and vascular optical coherence tomography for differentiating oral lesions of mice in different carcinogenesis stages," Biomed. Opt. Express **9**(4), 1461–1476 (2018).

13. C. K. Lee, T. T. Chi, C. T. Wu, M. T. Tsai, C. P. Chiang, and C. C. Yang, "Diagnosis of oral precancer with optical coherence tomography," Biomed. Opt. Express **3**(7), 1632–1646 (2012).

14. P. Pande, S. Shrestha, J. Park, M. J. Serafino, I. Gimenez-Conti, J. Brandon, Y. S. Cheng, B. E. Applegate, and J. A. Jo, "Automated classification of optical coherence tomography images for the diagnosis of oral malignancy in the hamster cheek pouch," J. Biomed. Opt. **19**(8), 086022 (2014).

15. V. Volgger, H. Stepp, S. Ihrler, M. Kraft, A. Leunig, P. M. Patel, M. Susarla, K. Jackson, and C. S. Betz, "Evaluation of optical coherence tomography to discriminate lesions of the upper aerodigestive tract," Head Neck **35**(11), 1558–1566 (2013).

16. S. Prestin, S. I. Rothschild, C. S. Betz, and M. Kraft, "Measurement of epithelial thickness within the oral cavity using optical coherence tomography," Head Neck **34**(12), 1777–1781 (2012).

17. M. T. Tsai, J. D. Lee, Y. J. Lee, C. K. Lee, H. L. Jin, F. Y. Chang, K. Y. Hu, C. P. Wu, C. P. Chiang, and C. C. Yang, "Differentiation of oral precancerous stages with optical coherence tomography based on the evaluation of optical scattering properties of oral mucosae," Laser Phys. **23**(4), 045602 (2013).

18. Y. F. Chen, C. C. Yang, S. Y. Kao, C. J. Liu, S. C. Lin, and K. W. Chang, "MicroRNA-211 Enhances the Oncogenicity of Carcinogen-Induced Oral Carcinoma by Repressing TCF12 and Increasing Antioxidant Activity," Cancer Res. **76**(16), 4872–4886 (2016).

19. X. H. Tang, B. Knudsen, D. Bemis, S. Tickoo, and L. J. Gudas, "Oral cavity and esophageal carcinogenesis modeled in carcinogen-treated mice," Clin. Cancer Res. **10**(1), 301–313 (2004).

20. W. C. Kuo, C. M. Lai, Y. S. Huang, C. Y. Chang, and Y. M. Kuo, "Balanced detection for spectral domain optical coherence tomography," Opt. Express **21**(16), 19280–19291 (2013).

21. H. Lin, M. C. Kao, C. M. Lai, J. C. Huang, and W. C. Kuo, "All fiber optics circular-state swept source polarization-sensitive optical coherence tomography," J. Biomed. Opt. **19**(2), 021110 (2013).

22. G. Liu, W. Jia, V. Sun, B. Choi, and Z. Chen, "High-resolution imaging of microvasculature in human skin in-vivo with optical coherence tomography," Opt. Express **20**(7), 7694–7705 (2012).

23. M. T. Tsai, H. C. Lee, C. K. Lee, C. H. Yu, H. M. Chen, C. P. Chiang, C. C. Chang, Y. M. Wang, and C. C. Yang, "Effective indicators for diagnosis of oral cancer using optical coherence tomography," Opt. Express **16**(20), 15847–15862 (2008).

24. S. Yousefi, J. Qin, Z. Zhi, and R. K. Wang, "Label-free optical lymphangiography: development of an automatic segmentation method applied to optical coherence tomography to visualize lymphatic vessels using Hessian filters," J. Biomed. Opt. **18**(8), 086004 (2013).

25. N. Otsu, "A threshold selection method from gray-level histograms," IEEE Trans. Sys., Man. Cyber. **9**(1), 62–66 (1979).

26. W. E. Hart, M. Goldbaum, B. Cote, P. Kube, and M. R. Nelson, "Measurement and classification of retinal vascular tortuosity," Int. J. Med. Inform. **53**(2-3), 239–252 (1999).

27. X. Liu, N. Xu, and A. Jiang, "Tortuosity entropy: a measure of spatial complexity of behavioral changes in animal movement," J. Theor. Biol. **364**, 197–205 (2015).

28. M. C. Downer, D. R. Moles, S. Palmer, and P. M. Speight, "A systematic review of test performance in screening for oral cancer and precancer," Oral Oncol. **40**(3), 264–273 (2004).

29. S. Warnakulasuriya, "Global epidemiology of oral and oropharyngeal cancer," Oral Oncol. **45**(4-5), 309–316 (2009).

30. H. M. Mehanna, T. Rattay, J. Smith, and C. C. McConkey, "Treatment and follow-up of oral dysplasia - a systematic review and meta-analysis," Head Neck **31**(12), 1600–1609 (2009).

31. E. C. Yang, M. T. Tan, R. A. Schwarz, R. R. Richards-Kortum, A. M. Gillenwater, and N. Vigneswaran, "Noninvasive diagnostic adjuncts for the evaluation of potentially premalignant oral epithelial lesions: current limitations and future directions," Oral Surg. Oral Med. Oral Pathol. Oral Radiol. **125**(6), 670–681 (2018).

32. P. Holmstrup, P. Vedtofte, J. Reibel, and K. Stoltze, "Oral premalignant lesions: is a biopsy reliable?" J. Oral Pathol. Med. **36**(5), 262–266 (2007).

33. M. Contaldo, A. Lucchese, E. Gentile, C. Zulli, M. Petruzzi, D. Lauritano, M. R. Amato, P. Esposito, G. Riegler, and R. Serpico, "Evaluation of the intraepithelial papillary capillary loops in benign and malignant oral lesions by in vivo Virtual Chromoendoscopic Magnification: a preliminary study," J. Biol. Regul. Homeost. Agents **31**(2 Suppl 1), 11–22 (2017).

34. A. Funayama, S. Maruyama, M. Yamazaki, K. Al-Eryani, S. Shingaki, C. Saito, J. Cheng, and T. Saku, "Intraepithelially entrapped blood vessels in oral carcinoma in-situ," Virchows Arch. **460**(5), 473–480 (2012).

35. S. C. Sarode and G. S. Sarode, "Better grade of tumor differentiation of oral squamous cell carcinoma arising in background of oral submucous fibrosis," Med. Hypotheses **81**(4), 540–543 (2013).

36. International Consortium for Outcome Research (ICOR) in Head and Neck Cancer, A. Ebrahimi, Z. Gil, M. Amit, T. C. Yen, C. T. Liao, P. Chaturvedi, J. P. Agarwal, L. P. Kowalski, M. Kreppel, C. R. Cernea, J. Brandao, G. Bachar, A. Bolzoni Villaret, D. Fliss, E. Fridman, K. T. Robbins, J. P. Shah, S. G. Patel, and J. R. Clark, "Primary tumor staging for oral cancer and a proposed modification incorporating depth of invasion: an international multicenter retrospective study," JAMA Otolaryngol Head Neck Surg. **140**(12), 1138–1148 (2014).

37. R. Murakami, S. Shiraishi, R. Yoshida, J. Sakata, K. Yamana, A. Hirosue, Y. Uchiyama, H. Nakayama, and Y. Yamashita, "Reliability of MRI-Derived Depth of Invasion of Oral Tongue Cancer," Acad. Radiol. **26**(7), e180–e186 (2019).

38. W. Hatta, K. Uno, T. Koike, S. Yokosawa, K. Iijima, A. Imatani, and T. Shimosegawa, "Optical coherence tomography for the staging of tumor infiltration in superficial esophageal squamous cell carcinoma," Gastrointest Endosc. **71**(6), 899–906 (2010).